Development and validation of an improved seismic velocity model for the San Jacinto fault region

PIs Clifford Thurber and Amir Allam

March 2017

Research accomplished

We have carried out a multi-faceted effort to improve the three-dimensional (3D) seismic velocity model for the region encompassing the San Jacinto fault zone (SJFZ) (Figure 1). P- and S-wave seismic velocity models have previously been determined for this region from separate inversions of body-wave arrival times by Allam and Ben-Zion (2012) for Vp and Vs and surface-wave dispersion data (from ambient noise) by Zigone et al. (2014) for Vs. These studies provided a starting point for our SCEC-supported work. The tasks that have been carried out consist of the following: (1) apply an effective automatic S-wave picker to an enlarged SJFZ waveform data set to provide data to further improve the sampling of the Vs structure; (2) develop ambient-noise surface-wave measurements at shorter and longer periods to provide increased constraint on the shallower and deeper structure, respectively, in the SJFZ region; (3) carry out joint body wave-surface wave inversions, including the addition of a substantial set of P-wave travel times from explosions to the earthquake dataset; (4) assess the validity of joint inversion models compared to the SCEC models by forward-modeling full-waveform data for a selected earthquakes.

(1) We assembled a set of waveforms for 6,432 earthquakes in the study region, 5,493 from Allam and Ben-Zion (2012) and 939 additional earthquakes. The automatic S-wave picker kpick (Rawles and Thurber, 2016) was applied to these waveforms. Based on tests performed with 2015 SCEC support, the S picks are expected to have errors less than 0.2 s more than 90% of the time. The processing yielded 78,602 new S-wave picks to combine with 105,488 existing S-wave picks. The number of P wave picks was also increased from 203,996 to 260,261. These are increases of 75% and 28%, respectively.

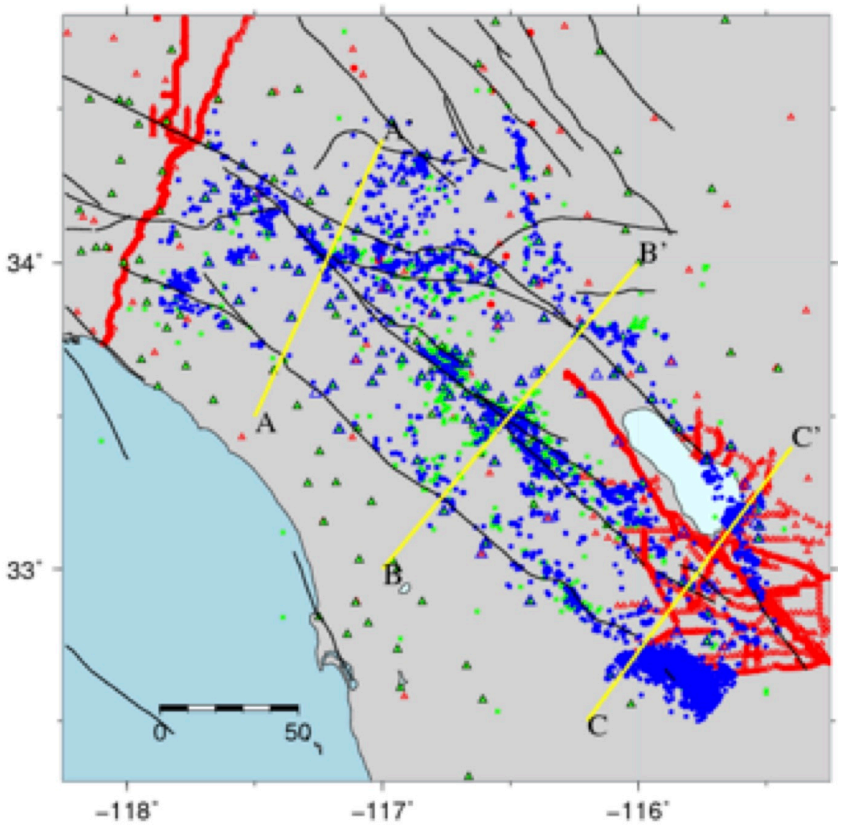

Figure 1. The new body-wave dataset. Circles represent earthquakes (blue: Allam and Ben-Zion (2012); green: new dataset) and shots (red). Stations are shown by triangles (blue: from Allam and Ben-Zion (2012); green: new dataset; red: refraction and temporary stations). Yellow lines indicate cross-sections shown in Figure 6. Faults are indicated by the black lines.

(2) Zigone et al. (2014) utilized surface wave dispersion data from ambient noise in the frequency range 3 to 12 s in their inversion for structure of the SJFZ region. Expanding the frequency range to shorter periods (down to 0.5 s) allows for improved resolution of shallow structure. Use of longer period (up to 20 s) data improves resolution at depth. The increase in Rayleigh wave group travel time data obtained by our expansion of the frequency range and analysis of additional data is indicated in Figure 2.

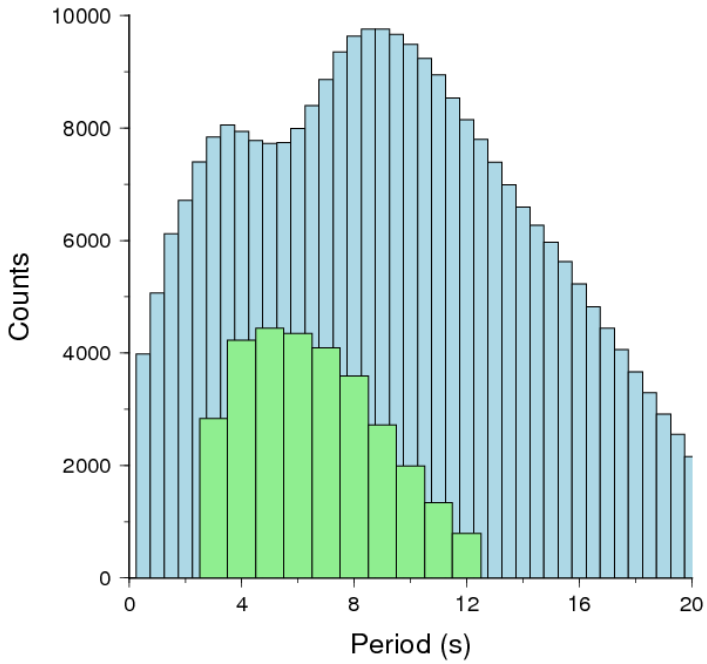

Figure 2. Comparison between the number of Rayleigh wave travel times between station pairs in the previous dataset versus the expanded dataset. The green bars represent the number of travel times in different frequency bins used by Fang et al. (2016), which were taken from Zigone et al. (2014). The blue bars represent the expanded dataset.

(3) We carried out joint inversions of the expanded body-wave and surface-wave datasets using the methods of Zhang et al. (2014) and Fang et al. (2016). The starting Vs model used (Figure 3) is from Fang et al. (2016). We included 94,968 P picks from 544 refraction shots, which have not previously been used for SJFZ region tomography studies (although some were used by Lin et al. (2010). The shot data are fit to 180 ms. Figure 4 shows the overall improvement in fit to both the body-wave and surface-wave data at each iteration of the joint inversion. The surface-wave part converges quickly, as it is closer to being a linear problem since it does not involve earthquake relocation, but the misfit reduction is modest (about 30%). The body-wave part converges more slowly, but shows a more substantial reduction in misfit (about 65%).

Cross-sections through the joint inversion model along the profiles indicated in Figure 1 are shown in Figure 5. Cross-section AA' lies between Profiles 2 and 3 of Allam and Ben Zion (2012) and shows similar features in the upper crust but lower velocities in the mid-crust in the northeastern part (X = 70 to 100 km) for both Vp and Vs. In cross-section BB', a shallow velocity low corresponding to Coachella Valley is evident at X = 80 km. The shallow low velocities of the Salton Trough are the most salient feature of profile CC' (near X = 80 km).

In Figure 6 we compare depth slices from the Fang et al. (2016) model to the new joint inversion results. For the P-wave model, the new model images much more of the structure along the coast. The new S-wave model appears somewhat more oscillatory compared to Fang et al. (2016), suggesting that our Vs smoothing weight may be slightly too small.

Checkerboard test results are shown in Figure 7. Compared to the Fang et al. (2016) checkerboard test results, resolution is substantially improved in the upper crust in our model.

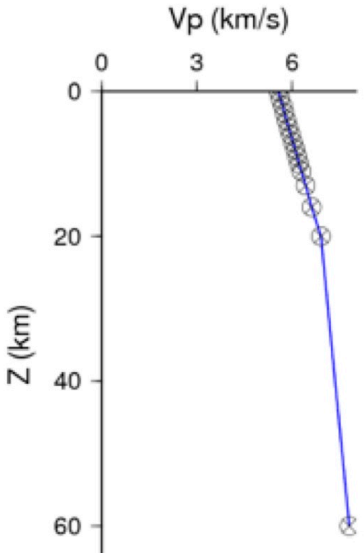

Figure 3. The starting Vp model and inversion nodes versus depth (crosses).

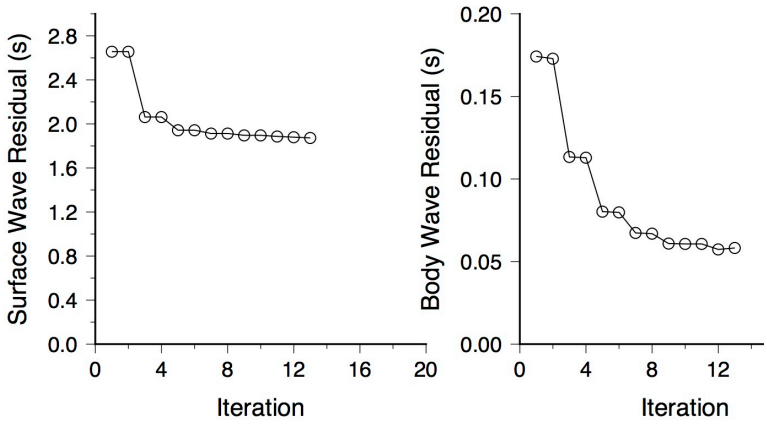

Figure 4. RMS residuals (in seconds) are shown for each iteration, (left) for surface waves, and (right) for body waves. The surface-wave and body-wave residuals are significantly reduced by the joint inversion.

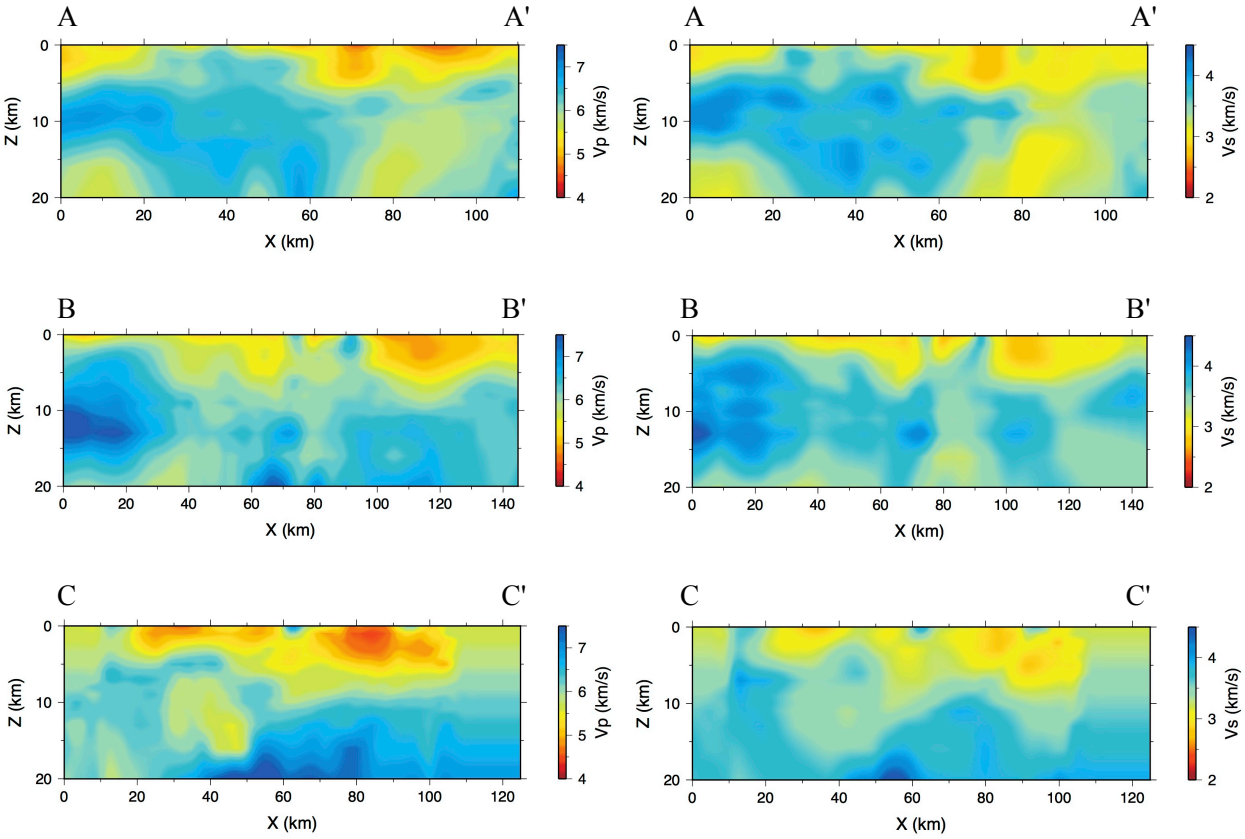

Figure 5. Cross-sections at AA', BB', and CC' (see Figure 1) for the (left) Vp and (right) Vs joint inversion models.

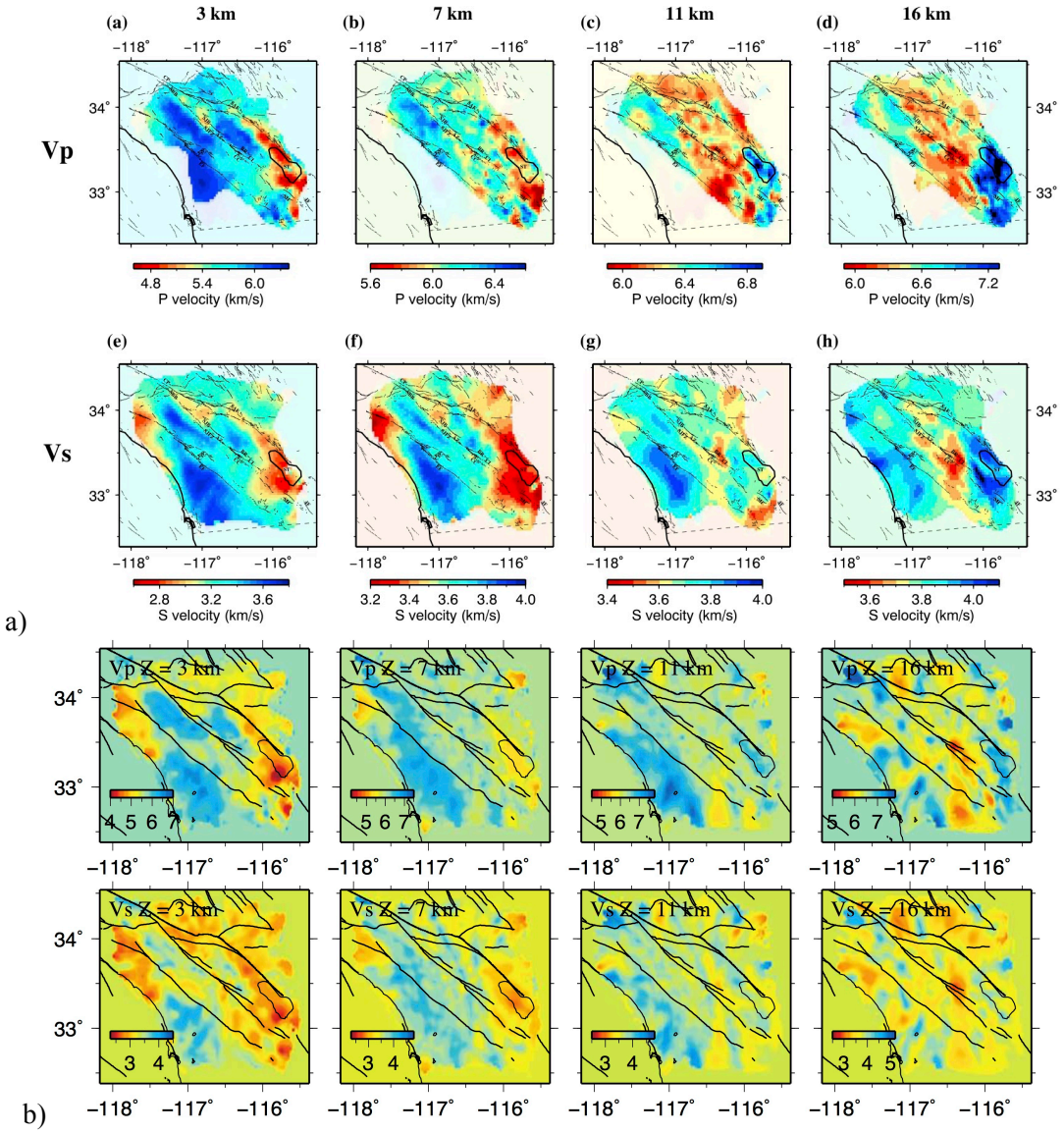

Figure 6. Comparison between the Fang et al. (2016) model and our new results. (a) Horizontal slices through the Fang et al. (2016) model for (top) Vp and (bottom) Vs at 3, 7, 11, and 16 km depth. (b) Horizontal slices through our new model for (top) Vp and (bottom) Vs at 3, 7, 11, and 16 km depth. Velocities in km/s.

(4) An example validation calculation is shown in Figure 8. The figure shows source and receiver geometry used for waveform simulations using the jointly-inverted model of Fang et al. (2016), the corresponding portion of which is also shown. The updated model (Figures 5 and 6) was not available in time for further comparisons. The focal mechanism was obtained using the Cut-And-Paste method. Synthetic waveforms computed in SPECFEM3D, low-pass filtered at 2 Hz, show that the body wave arrival times and amplitudes are well-matched, but surface wave amplitudes are underestimated. Time-frequency envelope misfit (Kristekova et al., 2006) for station KNW further illustrates that the P and S waves are generally well-matched, whereas the surface waves are fit poorly at low frequencies.

In addition, an undergraduate student at Utah has successfully produced 27 moment tensor solutions for M>5.0 events in southern California; we proposed to use 19 only events. These moment tensors are

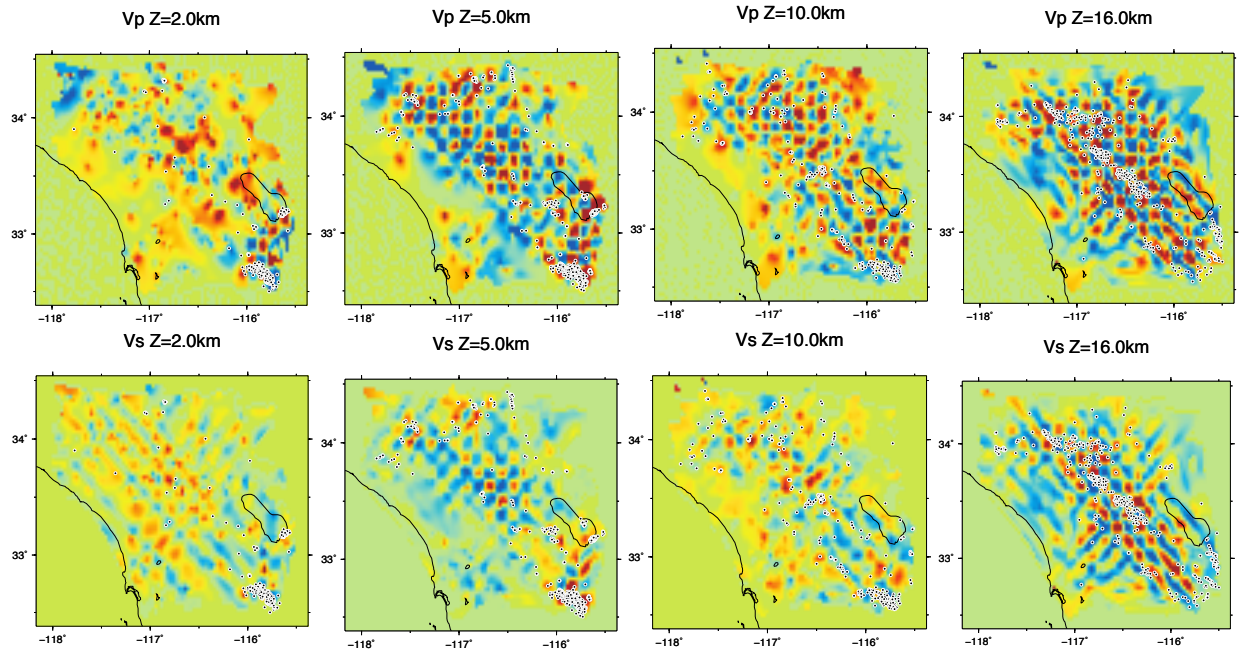

Figure 7. Recovered checkerboard model slices for the joint inversion using synthetic data and inversion parameters that match the real inversion. (top) Vp and (bottom) Vs recovered models. True anomaly amplitudes are ±4%.

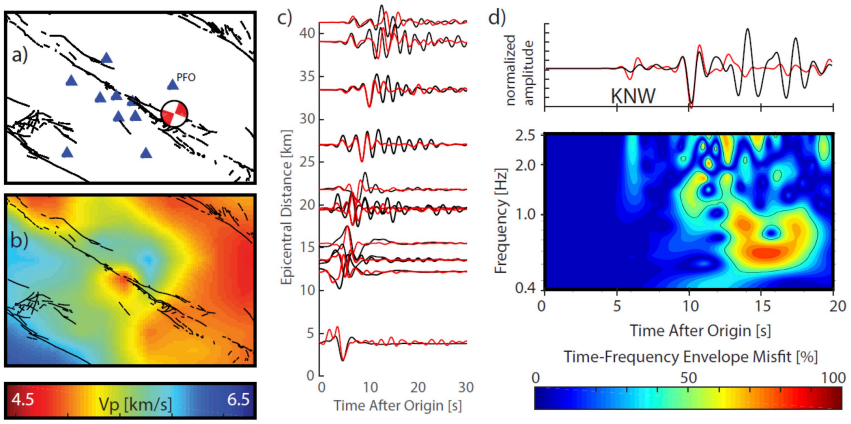

Figure 8. (a) Source and receivers for waveform simulations using (b) a jointly-inverted model. (c) Data (blue) and synthetic (red) waveforms from SPECFEM3D. (d) Time-frequency envelope misfit (Kristekova et al., 2006) for station KNW.

currently being used as sources for 3D simulations in the following velocity models: CVM-S4.26, CVMH, Fang et al. (2016), and the newest jointly-inverted velocity models. In addition, we have improved upon the original proposed waveform misfit quantification scheme, employing a method which measures misfit as a function of both time and frequency (Figure 8). Rather than a single value per waveform pair, this method provides the full misfit anatomy, showing not just how much the signals differ but also where. This distinction is especially useful for the southern California velocity models which tend to fit body waves extremely well, but often fail to fit surface waves.

Summary and recommendations

By expanding both the body-wave and surface-wave datasets, we have improved the sampling of the crust in the SJFZ region. In turn, this improves the resolution of the regional 3D seismic velocity structure obtained from a joint inversion of both data types. Further work should be done to assess the effectiveness of the updated model for matching observed seismograms using full waveform synthetics. We will provide our final model to SCEC researchers for such evaluation.

References

Allam, A., and Y. Ben-Zion (2012), Seismic velocity structures in the southern California plate-boundary environment from double-difference tomography, Geophys. J. Int. 190, 1181-1196.

Fang, H, H. Zhang, H. Yao, A. A. Allam, D. Zigone, Y. Ben-Zion, C. Thurber, and R. D. van der Hilst (2016), A new algorithm for three-dimensional joint inversion of body-wave and surface-wave data and its application to the Southern California Plate Boundary Region, J. Geophys. Res. Solid Earth, 121, doi:10.1002/2015JB012702.

IRIS DMC (2012), Data Services Products: ANCC-CIEI, Western US Ambient Noise Cross-Correlations, doi:10.17611/DP/ANCC.1.

Lin, G., C. H. Thurber, H. Zhang, E. Hauksson, P. M. Shearer, F. Waldhauser, T. M. Brocher, and J. Hardebeck (2010), A California statewide three-dimensional seismic velocity model from both absolute and differential times, Bull. Seism. Soc. Am., 100, 225-240.

Rawles, C., and C. Thurber (2015), A nonparametric method for automatic determination of P-wave and S-wave arrival times: Application to local microearthquakes, Geophys. J. Int. 202, 1164-1179, doi:10.1093/gji/ggv218.

Zhang, H., P. Roux, M. Maceira, and C. Thurber (2014), Joint inversion of body-wave arrival times and surface-wave dispersion for three-dimensional seismic structure around SAFOD, Pure Appl. Geophys. 171, doi: 10.1007/s00024-014-0806-y.

Zigone, D., Y. Ben-Zion, M. Campillo and P. Roux (2014), Seismic tomography of the Southern California plate boundary region from noise-based Rayleigh and Love Waves, Pure Appl. Geophys. 171, doi: 10.1007/s00024-014-0872-1.